Electronic Supplementary Information for

NiFe layered double hydroxide nanosheets array for high-efficiency electrocatalytic reduction of nitric oxide to ammonia

Ge Meng[a]*, Tianran Wei[b], Weijia Liu[b], Wenbo Li[b], Shusheng Zhang[c], Wenxian Liu[d], Qian Liu[e], Haihong Bao[f]*, Jun Luo[g], and Xijun Liu[b]*

a. Key Laboratory of Carbon Materials of Zhejiang Province, College of Chemistry and Materials Engineering, Wenzhou University, Wenzhou 325035, China. E-mail: mengge@wzu.edu.cn.

b. MOE Key Laboratory of New Processing Technology for Non-Ferrous Metals and Materials, and Guangxi Key Laboratory of Processing for Non-Ferrous Metals and Featured Materials, School of Resource, Environments and Materials, Guangxi University, Nanning 530004, China. E-mail: xjliu@tjut.edu.cn

c. College of Chemistry, Zhengzhou University, Zhengzhou 450000, China.

d. College of Materials Science and Engineering, Zhejiang University of Technology, Hangzhou 310014, China.

e. Institute for Advanced Study, Chengdu University, Chengdu 610106, Sichuan, China.

f. School of Chemical Engineering and Materials, Tianjin University of Science and Technology, Tianjin 300457, China. E-mail: bhhtjlg@163.com

g. Institute for New Energy Materials and Low-Carbon Technologies, School of Materials Science and Engineering, Tianjin University of Technology, Tianjin 300384, China.

Experimental Section

Synthesis

Preparation of NiFe-LDH/NSA and NiFe-LDH/NSP

According to the literature,[32] NiFe-LDH nanosheet arrays on Ni foam were prepared by a one-step ethylene glycol assisting hydrothermal method. Briefly, a piece of Ni foam was first ultrasonically washed in a 6 M HCl solution for 15 min in order to remove the NiO_x surface layers, and then rinsed with ethanol, acetone, and deionized (DI) water in sequence for several times. Next, 349 mg of $Ni(NO_3)_2 \cdot 6H_2O$, 161 mg of $Fe(NO_3)_3 \cdot 9H_2O$, and 120 mg of urea were subjected to a mixed solution of DI water (10 mL) and ethylene glycol (30 mL), which was then stirred for 30 min to totally dissolve. The solutions together with the acid-washed Ni foam were subjected to a 100 mL stainless-steel Teflon-lined autoclave, sealed, and maintained in an oven at 120 °C for 12 h. After cooling down, the sample (NiFe-LDH/NSA) was taken out, washed with DI water and absolute ethanol several times, and then dried in an oven at 80 °C overnight. The synthesis of NiFe-LDH/NSP was similar to the procedure of NiFe-LDH/NSA except for the absence of Ni foam.

Characterization

The morphology and the microstructure of the prepared as-synthesized samples were investigated by SEM (Quanta FEG 250), TEM (Talos F200X), and BET (MIC ASAP2460). The crystalline structures were characterized by Rigaku D/max 2500 X-ray diffractometer (XRD) with Cu Kα radiation (λ = 0.154598 nm). X-ray

photoelectron spectroscopy (XPS, ESCALAB 250Xi, Thermo Scientific) was carried with a monochromatic Al Kα radiation source.

NORR tests

All electrochemical measurements were carried out at room temperature (25 °C) in a typical H-type cell separated by an anion exchange membrane (Nafion 211) with an 0.1 M HCl solution containing 0.5 mM iron (II) sodium benzoate on an electrochemical workstation (CHI 760D). Before NRR tests, the Nafion membrane was pretreated by heating in 5 wt% H_2O_2 aqueous solution at 80 °C for 1 h and ultrapure water at 80 °C for another 1 h, respectively. The electrochemical experiments were carried out with an electrochemical workstation using a three-electrode configuration with the as-prepared electrodes, graphite rod, and SCE electrode as working electrode, counter electrode, and reference electrode, respectively. In this work, all potentials were *iR*-compensated and converted to the reversible hydrogen electrode (RHE) scale according to the Nernst equation. And the presented current density was normalized to the geometric surface area. All the polarization curves were the steady-state ones after several cycles. For NO reduction experiments, potentiostatic test were conducted in NO saturated 0.1 M HCl solution (50 mL) (the HCl electrolyte was purged with Ar for 30 min before the measurement). Pure NO (99.99 % purity) was continuously fed to the cathodic compartment using properly positioned spargers so that the whole cathode was hit by the gas bubbles. The plots of electrochemical impedance spectroscopy (EIS) were measured with 5 mV amplitude in a frequency of 0.01 Hz–10 kHz.

Quantification of NH_3

The quantity of ammonia produced was measured using a colorimetric method with indophenol blue reagent according to our previous work (*Angew. Chem. Int. Ed.* 2019, 58, 2321). To exclude possible NH_3 contaminant from air, we followed that once the catalysts, electrolytes, etc., were prepared and purified in earlier experiments making sure that NH_3 production cannot occur in Ar atmosphere, they should be protected in Ar atmosphere and ready for subsequent NORR experiment (*Small Methods* 2018, 3, 1800337). In addition, when NH_3 is quantified by a pectrophotometric method, the absorbance in the blank electrolyte should be deducted. The generated H_2 from the competing HER and the possible N_2O and N_2 by-products from NORR were quantified on a Gas chromatography (Agilent GC-7890). In this work, no N_2O and N_2 were observed.

Preparation of the working electrode

Typically, 3 mg of the as-prepared NiFe-LDH/NSP was dispersed in the mixed solution of 50 μL Nafion solution (5 wt%), 500 μL water and 450 μL isopropanol, followed by ultrasonic treatment to form a homogeneous ink. And then the catalyst ink was dropped on a Ni foam, and dried naturally at room temperature.

Zn–NO battery measurements

NiFe-LDH/NSA was directly employed as the cathode to initiate the NORR in the cathode chamber, and the polished Zn plate was used as the anode. A bipolar membrane was used to separate the cathodic and anodic chambers. During the discharge process, the Zn−NO electrochemistry implements NORR driven by Zn

dissolution. Similarly, a NiFe-LDH/NSP-loaded Ni foam (with a loading of 0.6 mg cm^{-2}) electrode was employed as the cathode to perform the NORR. The battery measurements with NiFe-LDH/NSP as the cathode are identical to the NiFe-LDH/NSP-based battery.

DFT calculations.

The VASP package with VASPKIT code were uesed to performed the DFT calculations. Generalized gradient approximation (GGA) with the Perdew-Burke-Ernzerhof (PBE) functional is employed to treat the exchange-correlation energy. The interaction between core and valence electrons was described by the projected augmented wave (PAW) basis set. the force convergence standard was set below 0.01 eV $Å^{-1}$.A converged cutoff was set to 400 eV and Polarization Correction were added. The 4 × 4 × 1 Monkhorst−Pack k-point mesh was used for each absorption models. The bottom two layers were fixed to implement the free energy calculation of each absorption models. A 15 Å vacuum layer was constructed along the z-axis for each model. Contributions of zero-point energies (ZPE), enthalpy and entropy were considered and calculated. In this work, the (001) surface model was chosen as the reaction surface since the (001) face (including (003) and (006) facets) is the major face in LDH according to our obtained XRD pattern (Figure S1). This is consistent with the literature (*Chem. Eng. J.* 2021, 403, 126297).

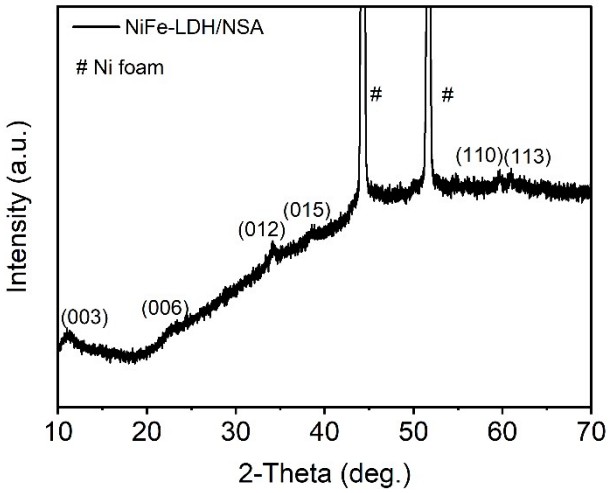

Fig. S1. XRD pattern of the as-prepared NiFe-LDH/NSA. Diffraction peaks at 11.4°, 22.97°, 34.43°, 38.99°, 59.94°, and 61.26° were observed, indexing to (003), (006), (012), (015), (110) and (113) planes of NiFe-LDH (JCPDS card No. 40-0215), respectively.

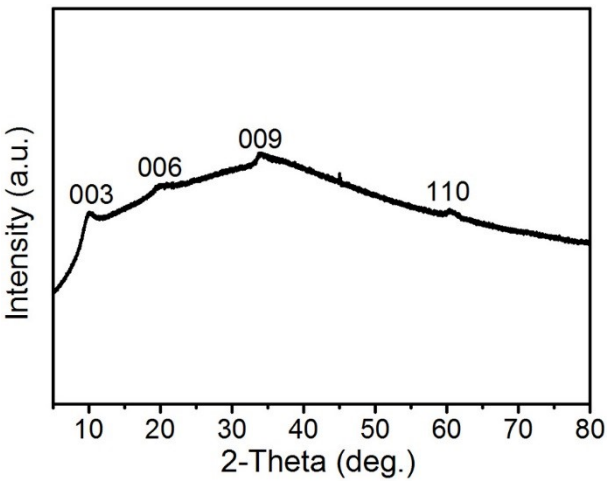

Fig. S2. XRD pattern of the as-prepared NiFe-LDH/NSP. All the diffraction peaks can be ascribed to NiFe-LDH (JCPDS card No. 40-0215).

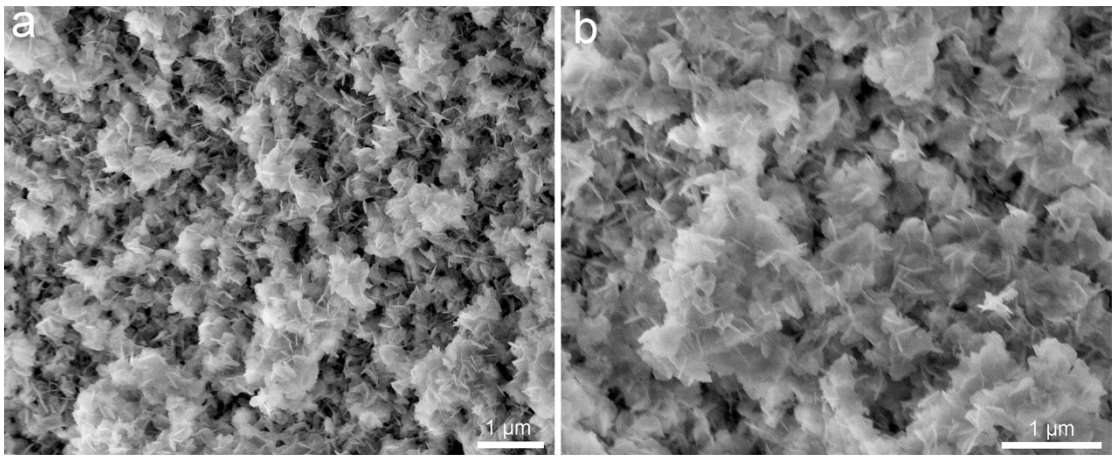

Fig. S3. SEM images of the as-synthesized NiFe-LDH/NSP.

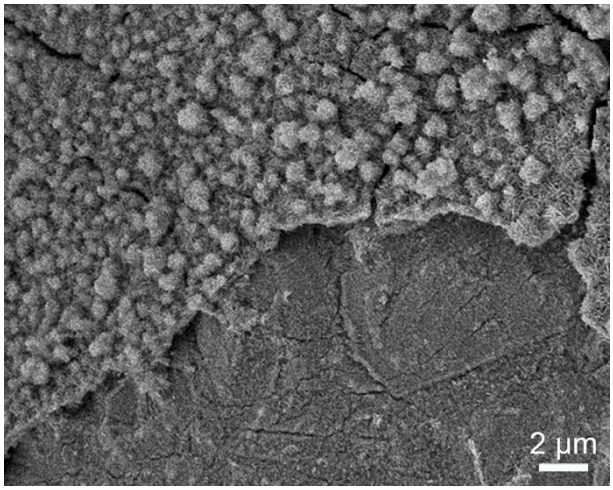

Fig. S4. SEM image of the as-synthesized NiFe-LDH/NSA.

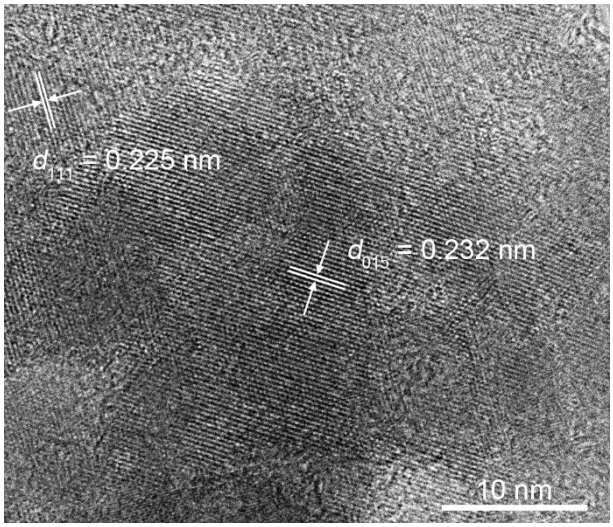

Fig. S5. HRTEM image of the as-synthesized NiFe-LDH/NSA.

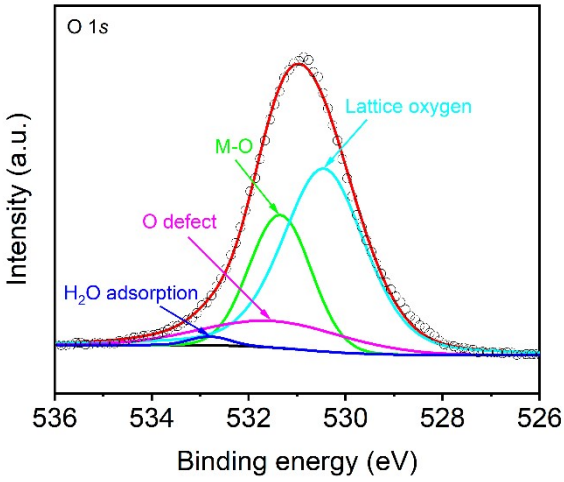

Fig. S6. High-resolution O 1*s* XPS spectrum of the as-synthesized NiFe-LDH/NSA.

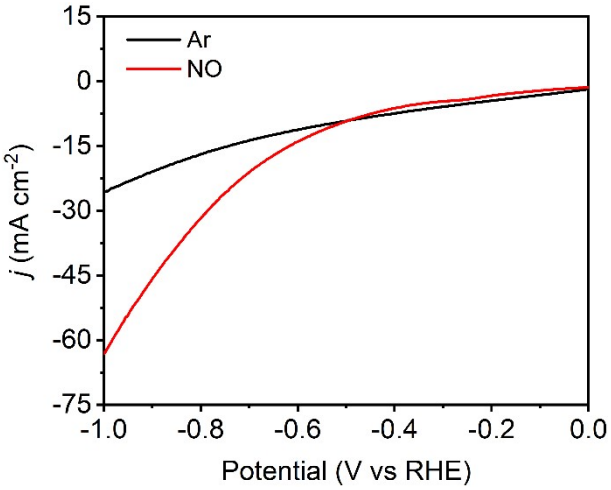

Fig. S7. NORR LSV curves of NiFe-LDH/NSA in Ar-/NO-saturated 0.25 M Li_2SO_4 electrolyte.

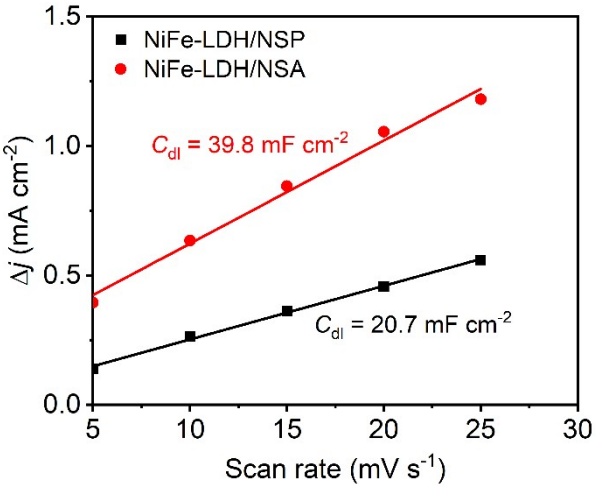

Fig. S8. Plots of current density versus the scan rate.

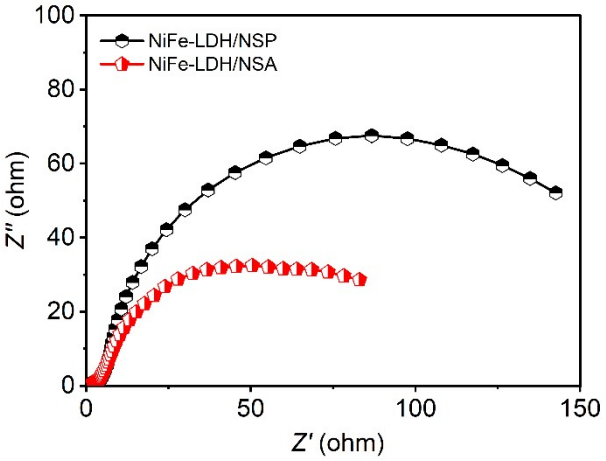

Fig. S9. EIS spectra of the as-synthesized NiFe-LDH/NSP and NiFe-LDH/NSA.

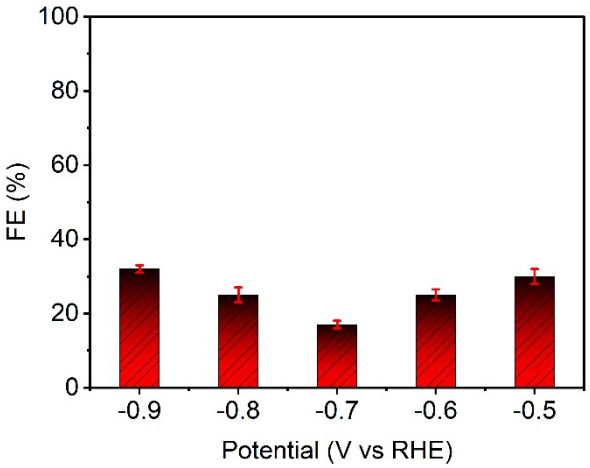

Fig. S10. The H_2 FE values recorded at different applied potentials. This result is consistent with theoretical analyses (Figure 4a). As seen, the ΔG_{H*} of NiFe-LDH is 0.69 eV, indicating its weaker binding with H (*Nature Commun.* 2022, 13, 1143). That is, the competing HER is effectively suppressed.

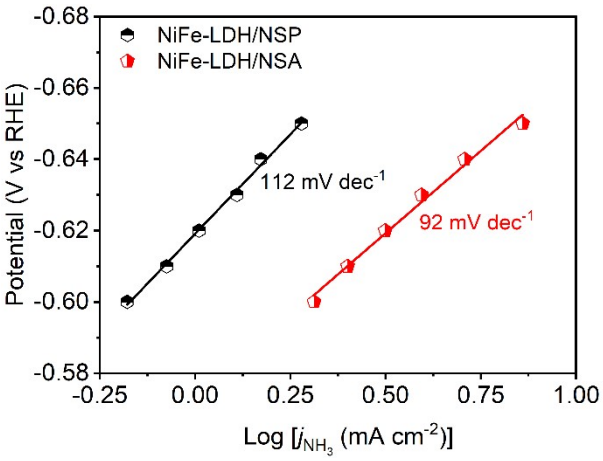

Fig. S11. Tafel plots for NiFe-LDH/NSP and NiFe-LDH/NSA.

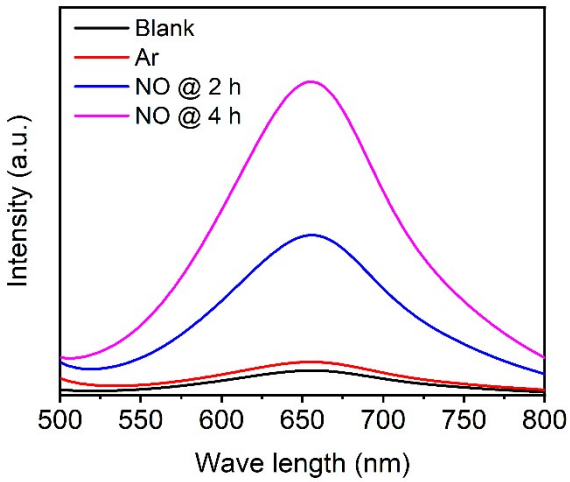

Fig. S12. UV-Vis spectra of different electrolytes catalyzed by NiFe-LDH/NSA in different reaction conditions.

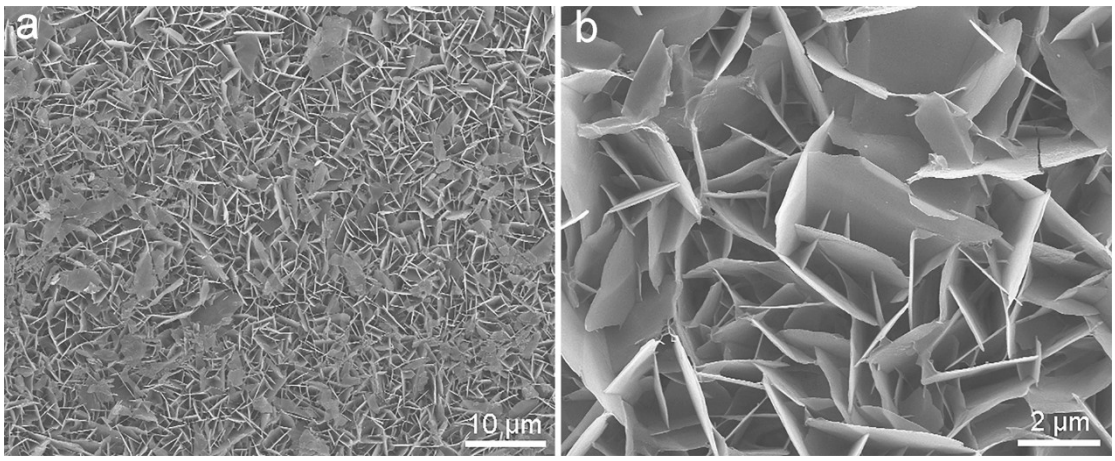

Fig. S13. SEM images of NiFe-LDH/NSA after the NORR electrolysis. It can be clearly seen that the morphology of NiFe-LDH/NSA is well preserved after the long-term electrolysis.

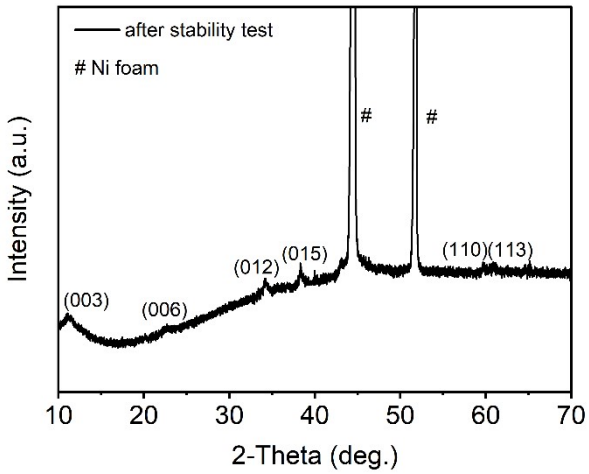

Fig. S14. XRD pattern of NiFe-LDH/NSA after the NORR electrolysis. Clearly, no additional diffraction peaks are observed.

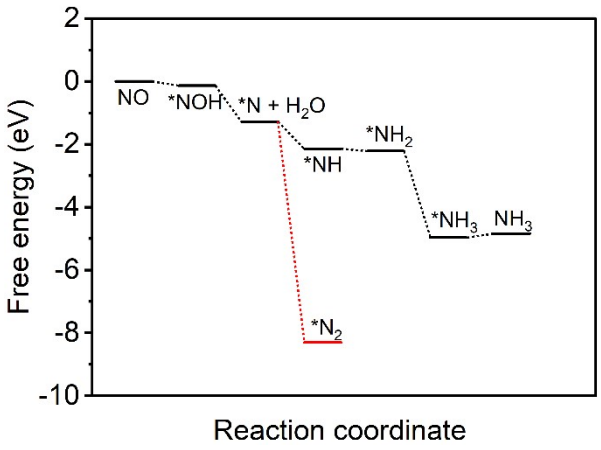

Fig. S15. The free energy changes for the NORR on NiFe-LDH (001) surface. As it can be seen that it is energetically unfavorable to make N–N coupling intermediates or products such as N_2, which is why we did not observe any N_2O or N_2 products from NO reduction on NiFe-LDH/NSA. Meanwhile, if any $*N_2O$ produced on NiFe-LDH (001), it will spontaneously decompose into N_2 and H_2O according to our calculations.

Table S1. Electrocatalysis results from this work and those reported NRR and NORR results in the literature.

Catalyst	Electrolyte	NH_3 Yield Rate	FE (%)	Potential	Reference
Au/TiO_2 Au (1.542 wt%)	0.1 M HCl	21.4 μg $h^{-1}mg_{cat.}^{-1}$	8.11	–0.2 V vs RHE	*Adv. Mater.* 2017, 29, 1606550
a-Au/CeOx-RGO Au (1.31 wt%)	0.1 M HCl	8.3 μg h^{-1} $mg_{cat.}^{-1}$	10.10	–0.2 V vs RHE	*Adv. Mater.* 2017;29, 1700001
THH Au NRs	0.1 M KOH	1.648 μg h^{-1} cm^{-2}	4.02	–0.2 V vs RHE	*Adv. Mater.* 2017, 29, 1604799
(110)-oriented Mo	Aqueous solutions	3.09×10^{-11} mol s^{-1} cm^{-2}	0.72	–0.49 V vs RHE	*J. Mater. Chem. A* 2017, 5, 18967
PEBCD/C	0.5 M Li_2SO_4	1.58 μg $h^{-1}cm^{-2}$	2.85	–0.5 V vs RHE	*J. Am. Chem. Soc.* 2017, 139, 9771
Fe_2O_3-CNT	0.1 M $KHCO_3$	2.2×10^{-3} g $h^{-1}m^{-2}$	4.9	–2.0 V vs Ag/AgCl	*Angew Chem. Int. Ed.* 2017, 56, 2699
$Pd_{0.2}Cu_{0.8}$/rGO	0.1 M KOH	2.8 μg h^{-1} $mg_{cat.}^{-1}$	~4.5	–0.2 V vs RHE	*Adv. Energy Mater.* 2018, 8, 1800124
N-doped porous carbon	0.05 M H_2SO_4	1.40 mmol g^{-1} h^{-1}	1.42	–0.9 V vs RHE	*ACS Catal.* 2018, 8, 1186

Au film	0.1 M KOH	3.84×10^{-12} mol cm^{-2} s^{-1}	<1	–0.5 V vs RHE	*J. Am. Chem. Soc.* 2018, 140, 1496
MOF-derived N-doped carbon	0.1 M KOH	3.4×10^{-6} mol h^{-1} cm^{-2}	10.2	–0.3 vs RHE	*Nano Energy* 2018, 48, 217
hollow Au nanocages	0.5 M $LiClO_4$	3.9 μg h^{-1} cm^{-2} (–0.5 vs RHE)	30.2	–0.4 vs RHE	*Nano Energy* 2018, 49, 316
RuPt/C	1 M KOH	1.04×10^{-8} g s^{-1} cm^{-2}	13.2	0.123 vs RHE	*Electrochem. Commun.* 2018, 90, 96
Boron-doped graphene	0.05 M H_2SO_4	9.8 μg h^{-1} cm^{-2}	10.8	–0.5 vs RHE	*Joule* 2018, 2, 1610
Amorphous $Bi_4V_2O_{11}/CeO_2$	0.1 M HCl	23.21 μg h^{-1} $mg_{cat.}^{-1}$	10.16	–0.2 vs RHE	*Angew Chem. Int. Ed.* 2018, 57, 6073
B_4C	0.1M HCl	26.57 μg h^{-1} $mg_{cat.}^{-1}$	15.95	–0.75 vs RHE	*Nat. Commun.* 2018, 9, 3485
Single Ru atoms	0.1 M HCl	120.9 μg h^{-1} $mg_{cat.}^{-1}$	29.6	–0.2 vs RHE	*Adv. Mater.* 2018, 0, 1803498.
$Ni_{0.75}Fe_{0.25}Se_2$	0.1 M Li_2SO_4	5.64 μg h^{-1} $cm_{cat.}^{-2}$	12.3	–0.1 vs RHE	*Inorg. Chem. Front.* 2021, 8, 1762
CoVP@NiFeV-LDH	0.05 M H_2SO_4	1.6 μmol h^{-1} cm^{-2}	13.8	–0.3 vs RHE	*Appl. Catal. B-Enviorn.* 2020, 265, 118559

SA-Mo/NPC	0.1 M KOH	34.0 ± 3.6 μg h^{-1} $mg_{cat.}^{-1}$ (34.0 ± 3.6 μg h^{-1} cm^{-2})	14.6 ± 1.6	–0.3 vs RHE	*Angew. Chem. Int. Ed. 2019, 58, 2321*
MoS_2/GF (NORR)	0.1 M HCl + 0.5 mM Fe(II)SB	99.6 μmol h^{-1} cm^{-2} (281.1 μg h^{-1} $mg_{cat.}^{-1}$)	76.6	–0.7 vs RHE	*Angew. Chem. Int. Ed. 2021, 60, 25263*
a-$B_{2.6}C$@TiO_2 (NORR)	0.2 M Na_2SO_4	3678.6 μg h^{-1} cm^{-2}	87.6	–0.9 vs RHE	*Angewandte Chemie International Edition, 2022, e202202087*
Cu foam (NORR)	0.25 Li_2SO4	517.1 μmol h^{-1} cm^{-2}	93.5%	–0.9 vs RHE	*Angew. Chem. Int. Ed. 2020, 59, 9711*
$Ru_{0.05}Cu_{0.95}$ (NORR)	0.2 M Na_2SO_4	17.68 μmol h^{-1} cm^{-2}	64.9	–0.5 vs RHE	*Sci. China Chem. 2021, 64, 1493*
Single atom Nb (NORR)	0.1 M HCl	295.2 μmol h^{-1} cm^{-2}	77.1	–0.6 vs RHE	*Nano Energy 2020, 78, 105321*
FeNC (NORR)	0.1 M $HClO_4$	~20.2 μmol h^{-1} cm^{-2}	~5.1	–0.2 vs RHE	*Nat. Commun. 2021, 12, 1856*
NiFe-LDH/NSA	0.25 M Li_2SO_4 + 0.1	112 μmol h^{-1} cm^{-2}	82	-0.7 vs RHE	*This work*

mM

Fe^{2+}–EDTA

Tbale S2. Comparison of NH_3 yield and power density of our battery with reported Zn-N_2 battery systems.

Catalyst	NH_3 yield rate	Power density	Reference
MoS_2/GF (Zn–NO)	411.8 μg h^{-1} $mg_{cat.}^{-1}$	1.04 mW cm^{-2}	*Angew. Chem. Int. Ed. 2021, 60, 25263*
$Fe_{1.0}$HTN (Zn–N_2)	0.172 μg h^{-1} cm^{-2}	0.02765 mW cm^{-2}	*J. Mater. Chem. A 2021, 9, 4026*
CoPi/HSNPC (Zn–N_2)	11.62 μg h^{-1} $mg_{cat.}^{-1}$	0.31 mW cm^{-2}	*J. Mater. Chem. A 2021, 9, 11370*
CoPi/NPCS (Zn–N_2)	14.7 μg h^{-1} $mg_{cat.}^{-1}$	0.49 mW cm^{-2}	*ACS Appl. Mater. Interfaces 2021, 13, 12106*
a-$B_{2.6}$C@TiO_2 (Zn–NO)	1125.2μg h^{-1} cm^{-2}	1.7 mW cm^{-2}	*Angewandte Chemie International Edition, 2022, e202202087*
NbS_2 (Zn–N_2)	NA	0.31 mW cm^{-2}	*Appl. Catal. B: Environ. 2020, 270, 118892*
Cu layer (Zn–N_2)	0.125 μg h^{-1} cm^{-2}	0.0101 mW cm^{-2}	*Chem. Commun. 2019, 55, 12801*
NiFe-LDH/NSA (Zn–NO)	32 μmol h^{-1} cm^{-2} 453.3 μg h^{-1} $mg_{cat.}^{-1}$	1.8 mW cm^{-2}	*This work*

Note: Indeed, the two kinds of Zn-based battery give rise to opportunities to generate NH_3 and release electricity simultaneously. Compared to N_2 reduction reaction, the NO molecule is more reactive than nonpolar N_2 and can be reduced more easily. As summarized in Table S2, great efforts have been devoted to develop Zn-N_2 batteries. By contrast, the construction of Zn-NO batteries has been rarely reported. Meantime, from Table S2, it can be found that the achieved power density and NH_3 yield rate on Zn-NO batteries significantly higher than those of Zn-N_2

batteries.